

Super-Keplerian Equatorial Outflows in SS 433 ★

Centrifugal Ejection of the Circumbinary Disk

Idel Waisberg¹, Jason Dexter¹, Pierre Olivier-Petrucci², Guillaume Dubus², and Karine Perraut²

¹ Max Planck Institute for extraterrestrial Physics, Giessenbachstr., 85748 Garching, Germany, e-mail: idelw@mpe.mpg.de

² Univ. Grenoble Alpes, CNRS, IPAG, F-38000 Grenoble, France

January 18, 2022

ABSTRACT

Context. The microquasar SS 433 is the only known steady supercritical accretor in the Galaxy. It is well-known for its relativistic baryonic jets, but the system also drives equatorial outflows. These have been routinely detected in radio images, and components associated with a circumbinary disk have also been suggested in optical emission lines.

Aims. We wish to spatially resolve the regions producing the stationary emission lines of SS 433 to shed light on its circumbinary structure and outflows. With an estimated binary orbit size $\lesssim 0.1$ mas, this requires optical interferometry.

Methods. We use the optical interferometer VLTI+GRAVITY to spatially resolve SS 433 in the near-infrared K band at high spectral resolution ($R \approx 4000$) on three nights in July 2017. This is the second such observation, after the first one in July 2016.

Results. The stationary Br γ line in the 2017 observation is clearly dominated by an extended ~ 1 mas ~ 5 AU circumbinary structure perpendicular to the jets and with a strong rotation component. The rotation direction is retrograde relative to the jet precession, in accordance with the slaved disk precession model. The structure has a very high specific angular momentum and is too extended to be a stable circumbinary disk in Keplerian rotation; interpreting it as such leads to a very high enclosed mass $M \gtrsim 400M_{\odot}$. We instead interpret it as the centrifugal ejection of the circumbinary disk, with the implication that there must be an efficient transfer of specific angular momentum from the binary to the disk. We suggest that the equatorial outflows sometimes seen in radio images result from similar episodes of circumbinary disk centrifugal ejection. In addition to the equatorial structure, we find a very extended ~ 6 mas ~ 30 AU spherical wind component to the Br γ line: the entire binary is engulfed in an optically thin spherical line emission envelope.

Key words. techniques: interferometric — binaries: close — stars: circumstellar matter — stars: winds, outflows — infrared: stars — stars: individual: SS 433

1. INTRODUCTION

The extreme emission-line object SS 433 (Stephenson & Sanduleak 1977; Clark & Murrin 1978) was the first microquasar discovered, from its broad, red/blueshifted hydrogen and helium emission lines moving across its optical spectrum (Margon et al. 1979) and produced by relativistic, precessing baryonic jets moving at $0.26c$ (Fabian & Rees 1979; Margon 1984). The jets are also seen in emission lines of highly ionized metals in X-rays (e.g. Marshall et al. 2013) and as moving knots (e.g. Vermeulen et al. 1993) and large-scale corkscrew structure in radio (e.g. Blundell & Bowler 2004). SS 433 is the only known Galactic manifestation of a *steady* super-Eddington accretion disk, which outshines its donor star at all wavelengths and drives powerful outflows, manifested not only in the jets but also in strong, broad and complex "stationary" (in wavelength) emission lines. The estimated mass outflow $\dot{M} \sim 10^{-4}M_{\odot}/\text{yr}$ (Shklovskii 1981; Fuchs et al. 2006) establishes SS 433 as an outflow-regulated supercritically accreting system ($\frac{\dot{M}}{\dot{M}_{\text{Eddington}}} \sim 500$ for a $10M_{\odot}$ black hole). For a review of SS 433's fascinating properties, see Fabrika (2004).

Although famous for its jets, one of the more exotic aspects of SS 433 are its equatorial outflows. The presence of an equa-

torial excretion flow from the accretion disk was proposed to explain the photometric and eclipsing behavior of SS 433 by Zwitter et al. (1991), possibly fed from the Lagrangian point behind the compact object (Fabrika 1993). The equatorial outflows were later detected in high-resolution radio images as outflowing emission knots at anomalous position angles, close to perpendicular to the jets (Paragi et al. 1999). Blundell et al. (2001) later detected a smooth, extended (~ 40 mas) equatorial structure in radio images, calling it the "radio ruff". A collection of further observations (Paragi et al. 2002; Mioduszewski et al. 2004) suggested that the orientation of the outflows is roughly perpendicular to but span a larger angle range ($\sim 70^\circ$) than the precessing jets ($\approx 40^\circ$) (Doolin & Blundell 2009).

On the other hand, the presence of equatorial, circumbinary material has also been inferred from the double-peaked shapes that often appear in the optical emission lines. Filippenko et al. (1988) ascribed the double peaks with half-separation ~ 150 km/s in the high-order Paschen lines to an accretion disk (deriving a rather low mass, suggestive of a neutron star, for the compact object), but also recognized that the structure may instead arise in a circumbinary disk that, if in Keplerian rotation, would imply a much larger $\gtrsim 40M_{\odot}$ enclosed mass. Robinson et al. (2017) presents a similar analysis of the higher-order Brackett lines, assigning them to an accretion disk and favoring a neutron star as the compact object. On the other hand, based on decomposing the line profiles with several different Gaussian

★ Based on observations collected at the European Southern Observatory, Chile, Program ID 099.D-0666(A).

components, Blundell et al. (2008) concluded that the $H\alpha$ emission line arises from a combination of a disk wind and a circumbinary disk, manifest as stable Gaussian components with half-separation ≥ 200 km/s. This velocity was interpreted as evidence that the total system mass must be large ($\geq 40M_{\odot}$) and the compact object must be a massive $\geq 16M_{\odot}$ black hole. Gaussian components arising from a circumbinary disk have also been suggested in the Br γ line (Perez M. & Blundell 2009) and again in $H\alpha$ and He I (Bowler 2010). Cherepashchuk et al. (2018) argues that the double-peaked structure must indeed arise from extended material because the wings of the line are not eclipsed (as would be expected for an accretion disk; SS 433 is an eclipsing binary). On the other hand, radial velocity measurements, notably extremely challenging in SS 433 due to the complexity of the emission lines and lack of clear stellar signatures, tend to favor lower masses $2 - 5M_{\odot}$ for the compact object (Hillwig & Gies 2008; Kubota et al. 2010). The relation between the circumbinary structure detected in optical emission lines and the equatorial outflows seen in radio is not clear. It has been suggested that the former might feed the latter (Blundell et al. 2008; Doolin & Blundell 2009).

With an orbital period $P_{orb} = 13.1$ days (Goranskii et al. 1998) and distance $d = 5.5$ kpc (Blundell & Bowler 2004), the semi-major axis of SS 433 is $a_{orb} = \left(\frac{M}{40M_{\odot}}\right)^{1/3} \times 0.07$ mas, where M is the total binary mass. Spatially resolving the optical emission requires sub-mas resolution. This is beyond the capabilities of even future extremely large telescopes, but is achievable through spectro-differential optical interferometry. In Gravity Collaboration et al. (2017b) (Paper I) we presented the first such observations taken during commissioning of the GRAVITY instrument (Gravity Collaboration et al. 2017a) in July 2016 at the Very Large Telescope Interferometer (VLTI), which works in the near-infrared K band. These observations spatially resolved the near-infrared continuum as well as the stationary double-peaked Br γ line. The interferometric signature across the latter showed a complex structure dominated by emission in the jet direction, suggestive of a bipolar outflow.

Here we report on a second set of observations of SS 433 with GRAVITY in July 2017, which clearly revealed equatorial emission with a strong rotation component. In Section 2, we summarize the observations and data reduction. The analysis of the K-band near-infrared continuum is presented in Section 3, whereas Section 4 describes the results on the stationary Br γ line. Finally, Section 5 presents the conclusions.

We often quote the results in mas since that is the actually measured unit. For convenience, we quote $1 \text{ mas} \leftrightarrow 8.23 \times 10^{13} \text{ cm} = 1180R_{\odot} = 5.5 \text{ AU}$, assuming a distance $d = 5.5(\pm 0.2)$ kpc derived from radio images using the aberration induced by light traveltime effect between the two jets (Blundell & Bowler 2004). The GAIA DR2 distance 4.6 ± 1.3 kpc (Luri et al. 2018) is consistent with this value.

2. OBSERVATIONS AND DATA REDUCTION

SS 433 ($K \approx 8$) was observed with GRAVITY (Gravity Collaboration et al. 2017a) with the Unit Telescopes (UT) on VLTI on three nights over a period of four days in July 2017. Half of the K band light of SS 433 itself was directed to the fringe tracker (FT), which operates at > 1000 Hz to stabilize the fringes in the science channel (SC), allowing coherent integration over detector integration times of 10s in high spectral resolution ($R \approx 4000$). The FT operates in low resolution ($R \approx 20$) with five channels over the K band. The data were obtained in split polarization

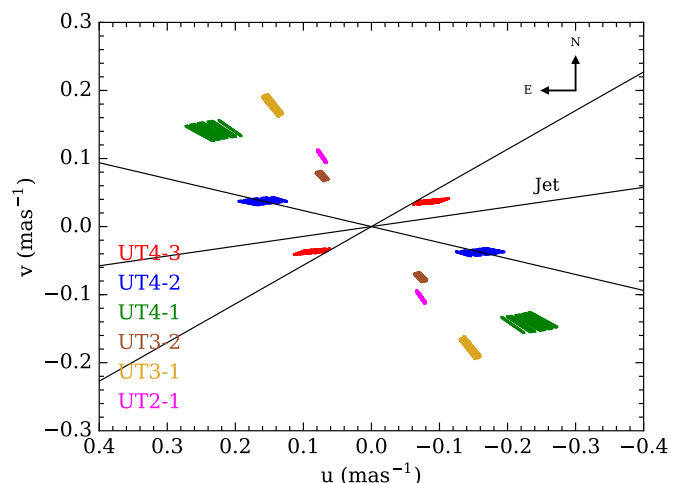


Fig. 1. The uv-coverage for Epoch 2 of the GRAVITY 2017 observations. The colors represent the six different baselines, and the coverage in the radial direction corresponds to the different wavelength channels across the K band ($2 - 2.5\mu\text{m}$). We also show the precessional axis of the jet and its precession cone as seen on sky. The projected baselines are sensitive to both the jet and the orthogonal directions.

mode. The adaptive optics (AO) was performed at visual wavelength using SS 433 itself as the AO guide star ($V \approx 14$).

Table 1 summarizes the observations. The precessional phase was ≈ 0.9 , when the disk inclination is close to its minimum value ($i \approx 60^\circ$). The orbital phases varied from $\approx 0.25 - 0.5$, so that the accretion disk is not eclipsed. Figure 1 shows the uv coverage for second observation epoch, with the jet precessional axis and cone as seen in radio observations (e.g. Stirling et al. 2002). The uv coverage for the other epochs is similar, but shorter in the third observation. The imaging resolution is ≈ 3 mas; however, we can resolve structures at sub-mas resolution through spectral differential visibilities.

The data were reduced with the standard GRAVITY pipeline (version 1.0.7, Lapeyrere et al. 2014). The interferometric calibrators used are listed in Table 1. They were also used as telluric line calibrators. We detected no significant difference in the interferometric quantities between the two polarizations in any of the three nights, either in the continuum FT or differential SC visibilities, and therefore we averaged the two polarizations. The data is also averaged in time for each of the three epochs because we do not see clear variability during each observation. We use the low resolution FT data to study the K band continuum, and the high resolution SC data to study the emission lines through differential visibility amplitudes and phases. Our limited uv coverage resulting from the rather short observations did not allow for model-independent image reconstruction; therefore, we have to rely on model-independent quantities and model fitting.

3. The Near-Infrared K band Continuum

SS 433 is known to have strong infrared excess (e.g. Allen 1979; Fuchs et al. 2006) from extended outflows. At NIR wavelengths, we expect a flux contribution from both the accretion disk and donor star ($\ll 0.1\text{mas}$) and from more extended emission. In all observations, the continuum closure phases are very small $\leq 2^\circ$, pointing to symmetric structures within our spatial resolution ≈ 3 mas.

In Paper I we reported a phenomenological model for the K band continuum consisting of a partially resolved source

Table 1. Summary of observations.

Date Time(UTC)	Total Integration Time (min)	Seeing (")	Coherence Time @ 500 nm (ms)	Calibrator ^a Spectral Type Diameter (mas)	Jet Precessional Phase ^c	Orbital Phase ^d
2017-07-07 6:25-8:10 Epoch 1	70	0.4-0.6	4-6	HD 183518 A3V 0.157 ± 0.002	0.895	0.252
2017-07-09 6:35-8:10 Epoch 2	60	0.5-0.7	8-13	HD 185440 A2/3V ^b 0.218 ± 0.002	0.907	0.405
2017-07-10 6:25-6:55 Epoch 3	20	0.4-0.5	7-9	HD 188107 B9V 0.173 ± 0.002	0.913	0.480

Notes.

^(a) Based on Chelli et al. (2016).

^(b) This calibrator is probably misclassified as it has strong CO bands in its spectrum.

^(c) Based on the kinematic parameters in Eikenberry et al. (2001). Phase zero is when the eastern/western jet is maximally blue/redshifted.

^(d) Based on the orbital parameters in Goranskii et al. (1998). Phase zero corresponds to the eclipse center of the accretion disk.

(FWHM $\lesssim 1$ mas) embedded in a completely resolved background with $\approx 10\%$ of its flux. Here we construct a slightly more involved model in face of the strong evidence for an equatorial structure in the 2017 observations. The model consists of two components: an unresolved point source representing the binary (accretion disk + donor star) and a two-dimensional elliptical Gaussian which could represent an extended disk/wind. The model parameters are:

1. the flux ratio f between the Gaussian and the point source components;
2. the FWHM θ_g of the Gaussian component along the major axis;
3. the disk inclination i , which gives the aspect ratio of the Gaussian $\cos(i)$;
4. the position angle (PA) of the Gaussian axis.

The model visibility is therefore:

$$V(\mathbf{u}) = \frac{1 + f \times V_{\text{gaussian}}(\mathbf{u})}{1 + f} \quad (1)$$

where V_{gaussian} is the visibility of the elliptical Gaussian and $\mathbf{u} = \frac{\mathbf{B}}{\lambda}$ with \mathbf{B} the baseline vector.

Table 2 and Figure 2 show the results for the model fits to the continuum squared visibilities for the 2016 observation and Epoch 2 of the 2017 observations (the other epochs look similar). Because the measurement errors are dominated by systematics from imperfect calibration of the visibilities (which leads to large χ^2_{dof}), we estimate the parameter errors from bootstrapping over the different baselines. We also note that spectral channels with strong emission lines were not used, to avoid the biasing of continuum visibilities by the differential visibilities.

The model fits point to an extended structure with a FWHM ~ 7 mas containing 10 – 30% of the flux of the central point source. The PAs are very not well-constrained, but the inclinations do not favor a symmetric Gaussian. The extended continuum structure could therefore correspond to a disk, with some possible contribution from an extended wind (both of which are

seen in the Bry line, see below). The inclination and position angle of the jets are $i_{\text{jet}} \approx 90^\circ$, $PA_{\text{jet}} \approx 75^\circ$ in the 2016 observation (Paper I) and $i_{\text{jet}} \approx 60^\circ$, $PA_{\text{jet}} \approx 88^\circ$ for the 2017 observations (see companion paper on the jets, Waisberg et al. sub.).

4. The Stationary Bry line

The K band spectrum

The K band spectrum of SS 433 contains both stationary emission lines (Bry, He I 2.06 μm , He I 2.112 μm and high order (upper levels 19-24) Pfund lines) as well as emission lines from the baryonic jets. By far the strongest stationary line is the Bry line, which is the focus of this paper. It is a broad line with FWHM ~ 1000 km/s and often shows a double peaked structure. We note that the Bry stationary line in our observations is partially blended with Pa α emission lines from the receding jet. Figure 4 shows the relevant part of the K band spectrum for Epoch 2, with velocities centered on the Bry line. For the complete K band spectra, we refer to the companion paper on the jets (Waisberg et al. sub.).

Model-independent Results

As mentioned previously, the stationary emission lines in SS 433 have been ascribed to multiple components, including an accretion disk, extended accretion disk wind/outflow and circumbinary ring. Our interferometric data *spatially* resolve the Bry line emission for the first time. The differential phases on most baselines show a remarkable "S-shape", which is a typical signature of a spatial velocity gradient (Figure 4). A comparison of the differential phases between the jet lines and the Bry line reveals that in 2017 the latter is perpendicular to the jets, rather than along their direction as was the case in the 2016 observation (Paper I). This can be clearly visualized in a model-independent way by converting the differential phases $\Delta\phi$ to centroid offsets Δx

Table 2. K Band Continuum Model Fit Results

Parameter	unit	2016-07-17	2017-07-07 Epoch1	2017-07-09 Epoch2	2017-07-10 Epoch3
f	-	0.20 ± 0.01	0.10 ± 0.01	0.15 ± 0.01	0.28 ± 0.01
θ_g	mas	7 ± 1	7 ± 1	9 ± 2	7 ± 1
i	deg	90 ± 27	48 ± 16	60 ± 13	90 ± 14
PA	deg	22 ± 58	98 ± 39	103 ± 43	12 ± 63
$\frac{\chi^2}{dof}$		60	102	42	127

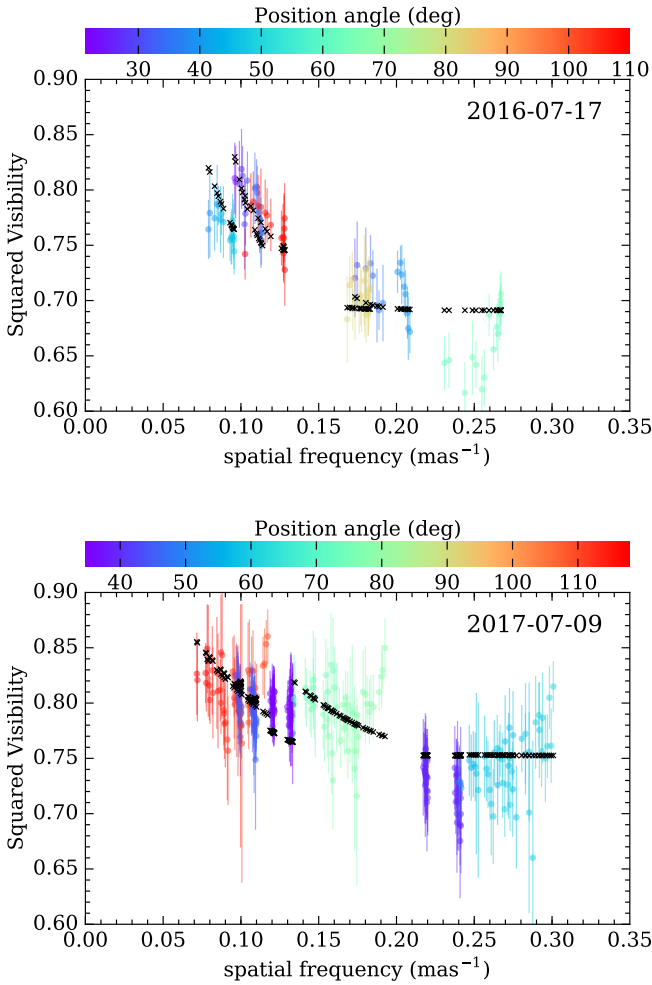


Fig. 2. K band continuum squared visibilities of SS 433 from the GRAVITY fringe tracker for the 2016 observation (**top**) and Epoch 2 of the 2017 observation (**bottom**). It is modeled by the combination of an unresolved point source representing the binary (accretion disk + donor star) and a two-dimensional elliptical Gaussian which could represent an extended disk/wind. The data is shown in color and the best fit model is shown in black.

between the line and the continuum, since in the marginally resolved limit (e.g. Monnier & Allen 2013; Waisberg et al. 2017):

$$\Delta\phi = -2\pi\mathbf{u} \cdot \Delta\mathbf{x} \left(\frac{f-1}{f} \right) \quad (2)$$

where $\mathbf{u} = \frac{\mathbf{B}}{\lambda}$ and f is the line flux in continuum-normalized units. Figure 3 shows the centroid of emission across the Bry line for the 2016 observation (Paper I) and Epoch 2 of the 2017 observations, along with the centroid of the jet emission lines. The emission is dominated by a bipolar (jet-like) structure in the 2016 observation, as reported in Paper I (although with a substantial scatter and an apparent offset ≈ 0.2 mas between the jet PA and the stationary line PA), and by a clear equatorial structure in the 2017 observation.

Figure 4 shows the interferometric data of Epoch 2 of the 2017 observations on two representative baselines (one close to perpendicular to the jets, the other close to parallel to the jets). We note the following important findings:

1. From Figure 3, the higher velocity part of the line is more compact than the lower velocity, which points to a significant rotation component rather than a radially accelerating outflow;
2. Figure 4 shows that the differential phase peaks, which are much stronger in baselines closer to perpendicular to the jets, have a half-separation of ~ 250 km/s, and extend to ≥ 1000 km/s. The jet inclination in SS 433 is $\geq 60^\circ$, so that any disk-like component is likely to be very close to edge-on, so that this velocity should be close to the deprojected velocity;
3. From Figure 3, the centroid displacement near the line peak (where the differential phase peaks occur) is ≥ 0.4 mas. This is a lower limit to the size of the region associated with that intrinsic velocity because, in a disk, projection effects cause inner material to also contribute to that velocity. We also note that, if the emission line has additional components so that the true f is reduced, the centroid displacement necessary to produce the same differential phase will be larger. Therefore, 0.4 mas is a lower limit to the size of the region where the velocity is ~ 250 km/s.

This clearly shows that the rotating structure is too extended to be an accretion disk, since $a_{orb} < 0.07$ mas for a total binary mass $M < 40M_\odot$. The phase peaks ~ 250 km/s are close in velocity to the Gaussian components that have been associated with a circumbinary ring in previous spectral decompositions (Blundell et al. 2008; Bowler 2010); however, the interferometric data show that these structures are too extended to correspond to the inner edge of a circumbinary ring at $\approx 2a_{orb}$. We note that the Keplerian velocity $v_{Kep} = \sqrt{\frac{GM}{r}}$ at 0.4 mas for $M < 40M_\odot$ is ≈ 130 km/s, so that if in Keplerian rotation the structure would imply a very high enclosed mass $\geq 150M_\odot$. Alternatively, the structure may be an equatorial rotating outflow (see below).

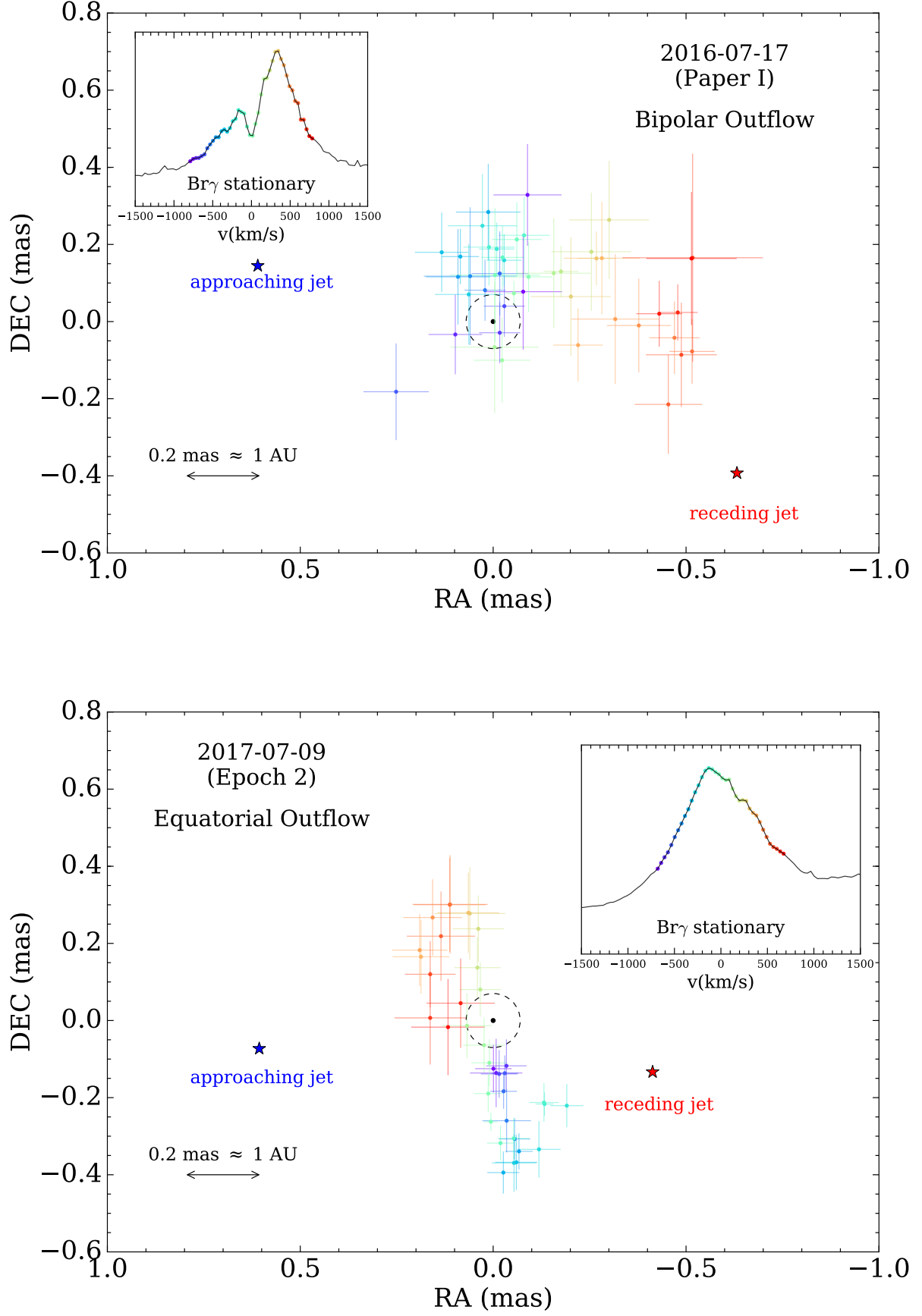


Fig. 3. Model-independent centroid shifts across the Br γ stationary line for the 2016 observation and Epoch 2 of the 2017 observations. The dashed circle shows the binary size $a \approx 0.07$ mas for a total mass $M = 40M_{\odot}$. The insets show the Br γ line spectrum with the color corresponding to the different wavelength/velocity channels.

Models

We model the equatorial structure emitting in Br γ as a geometrically and optically thin disk-like structure, which can be either stationary in Keplerian rotation or expanding. The parameters are as follows:

1. The outer radius R_{out} (mas), beyond which Br γ emission ceases;
2. The ratio of outer to inner radius $\frac{R_{out}}{R_{in}}$, the latter demarcating the radius at which Br γ emission begins;
3. The radial emission profile in Br γ , parametrized by $I(r) \propto r^{-\alpha}$;
4. The deprojected rotation velocity at the outer radius, $v_\phi(R_{out})$. The rotational velocity is given by

$$v_\phi(r) = v_\phi(R_{out}) \left(\frac{R_{out}}{r} \right)^\beta \quad (3)$$

where $\beta = 0.5$ for Keplerian rotation and $\beta = 1$ for an expanding outflow from conservation of angular momentum.

5. The outflow velocity v_r for the case $\beta = 1$. This is assumed to be constant i.e. the outflow has reached its terminal velocity by the time Br γ emission starts.
6. The inclination i of the disk;
7. The position angle PA of the disk;
8. The systematic velocity of the disk, v_{sys} , which could include e.g. orbital motion;
9. The turbulence velocity fraction, given by $\sigma = \frac{v_{turb}}{v_\phi}$. This parameter makes the double-peaked profile typical of disks less pronounced.

In addition, there is a need for an extended component, which also creates the high velocity $\gtrsim 1000$ km/s wings of the line profile. This is because the differential visibility amplitudes decrease across the line, pointing to a net structure that is more extended than the continuum, whereas the disk alone would cause an increase in visibility amplitude if no other component were present (Figure 4). The presence of a broad wind component agrees with previous spectroscopic decompositions of the stationary lines (e.g. Blundell et al. 2008; Perez M. & Blundell 2009). We model it as a spherically symmetric component, assumed to produce a Gaussian emission line in the spectrum and a symmetric 2d Gaussian in the image. Since it is spherically symmetric, this component does not induce differential visibility phase shifts. Its model parameters are:

1. The strength and FWHM (km/s) of the wind line in the spectrum, FWHM_{wind} ;
2. The size (FWHM) of the wind image (mas), θ_{wind}

The systemic velocity is assumed to be the same as for the equatorial structure.

The errors for the science channel are estimated from the scatter in line-free regions. We fit for the spectrum and the differential visibilities simultaneously; however, because the former is sensitive to telluric correction and has very small statistical error bars, we increase the flux error bars by a factor of two. We find that this scaling led to a comparable reduced χ^2 between flux and visibilities in all observations. Moreover, because of the blending with Pa α emission lines from the receding jet, which also produces differential visibility signatures, it is necessary to perform simultaneous fits for the Br γ line and the jets. For the

model and results for the jets we refer to the companion paper (Waisberg et al., sub.).

For the velocity-resolved interferometric model for the equatorial disk detailed above, we construct a spatial grid with velocities and fluxes determined by the model parameters, and the visibilities are then computed through a numerical 2D Fourier transform. The total differential visibility at a given spectral channel is then

$$V_{diff}(\mathbf{u}) = \frac{V(\mathbf{u})}{V_c(\mathbf{u})} = \frac{1 + \sum_i \frac{V_i(\mathbf{u})}{V_c(\mathbf{u})} f_i}{1 + \sum_i f_i} \quad (4)$$

where V_c is the continuum visibility (taken from the best fit continuum model, Section 3), and f_i and V_i are the flux ratios relative to the continuum and visibilities for each component i (equatorial disk/outflow, extended wind and jets).

The fits are done through non-linear least squares minimization with the Levenberg-Marquardt method through the python package LMFIT¹. The quoted errors correspond to the 1- σ errors from the least squares fit i.e. the estimated derivatives around the optimal solution (scaled by $\sqrt{\chi^2_{red}}$). We caution, however, that true uncertainties are dominated by (i) degeneracies between the many parameters, which create a complicated multi-dimensional χ^2 map; (ii) systematic errors from the continuum model; (iii) the assumption of our simple "geometric" models, which cannot capture all the complexities involved. A more realistic assessment of the errors can probably be grasped from the comparison between the results of the three different epochs (barring fast variability). We note, however, that in Epoch 1 there is very severe spectral blending of the different components, so that its results are less robust.

Model Results

Table 3 shows the model fit results for both the disk and outflow models. Figure 4 shows the data and best fit for the "outflow" model in Epoch 2 for two representative baselines. All the data and best fits for the three epochs for "outflow" model are shown in the Appendix.

The PA of the equatorial structure is close (although not exactly) perpendicular to the jets (the fit jet PA is 88° , see the companion paper on the jets, Waisberg et al., sub.), confirming the results from the model-independent analysis. The inclination of the outflow is also close to the jet inclination during the observations (60°). Interestingly, the rotation direction of the equatorial outflow is retrograde relative to the jet precession (known from radio and optical observations), in agreement with the slaved disk precession model, according to which the precession is driven from gravitational torques from the compact object on a donor star with a spin axis misaligned with the binary plane (Roberts 1974; van den Heuvel et al. 1980; Whitmire & Matese 1980). Modeling of the eclipses in the X-ray and optical light curves at different precessional phases had shown evidence of retrograde precession (e.g. Brinkmann et al. 1989; Leibowitz 1984); our results clearly confirm that the jets precess retrograde relatively to the binary.

The "disk" and "outflow" models look very similar and cannot be distinguished based on the χ^2 . However, we disfavor the "disk" model based on the following arguments. The resulting enclosed mass is very high $\sim 400M_\odot$, which follows from the

¹ <https://lmfit.github.io/lmfit-py/>

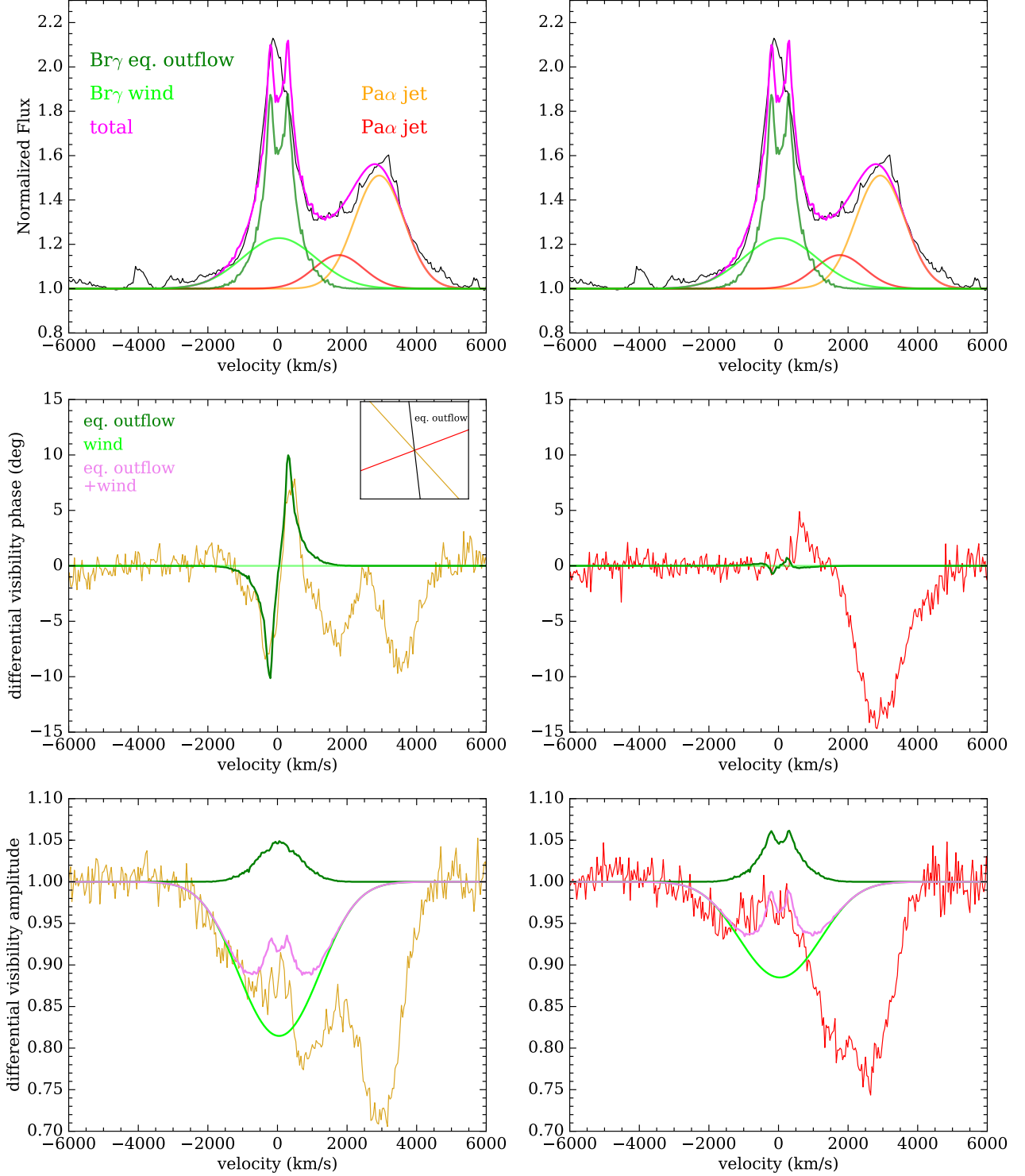


Fig. 4. This figure illustrates the main features of the data and model. We show two representative baselines (UT3-1, yellow and UT4-3, red – see Figure 1) for Epoch 2 and the outflow model fit. The **top** row shows the spectrum centered on the $\text{Br}\gamma$ stationary line. The latter is decomposed into an equatorial outflow (dark green) and a spherical wind (lime). The former is responsible for the S-shape signatures in the differential visibility phases (**middle** row) for baselines which are close to perpendicular to the jet (left), and show almost no signature on baselines more aligned with the jet (right). The inset shows the position angle of the outflow from the fit as well as the baseline directions on the sky plane. The **bottom** row shows the differential visibility amplitudes. The equatorial outflow alone would lead to an increase in visibility amplitude across the $\text{Br}\gamma$ line. The extended wind component can explain both the high velocity wings ≥ 1000 km/s in the spectrum as well as the net decrease in visibility amplitude across the line. Note that there are two $\text{Pa}\alpha$ emission lines from the receding jet which are blended with the $\text{Br}\gamma$ stationary line on its red side, and which also create strong visibility signatures. The model fits were done for all the components simultaneously, but here we show only the visibility model for the stationary line for clarity (full model is shown in the Appendix). For the jet model and results, we refer to the companion paper on the jets (Waisberg et al., sub.)

fact that the disk is too extended $R_{out} \approx 1$ mas for its velocity $v_\phi(R_{out}) \approx 260$ km/s. It would entail that SS 433 harbors an intermediate mass black hole, which is strongly disfavored by all that is known about the object, such as the radial velocity curves and eclipse behavior (Fabrika 2004). Even more problematic is the fact that the "disk" model is not self-consistent: for such a high mass, $a_{orb} \sim 0.15$ mas, which is larger than the resulting inner radius $\lesssim 0.1$ mas; therefore, the disk would have to pass through the binary orbit.

Instead, we favor the "outflow" model. In this case, the extended equatorial structure we detect would correspond to an outflow moving out at $v_r \sim 240$ km/s but with a very significant rotation component. The inner edge of the outflow at ~ 0.1 mas has a rotational velocity ~ 1500 km/s and the outer edge at ≈ 0.7 mas rotates at ≈ 220 km/s. This corresponds to a very high specific angular momentum, which is $\gtrsim 10$ times larger than the specific orbital angular momentum of the compact object l_X for a total mass $M < 40M_\odot$, assuming a radial velocity amplitude $K_X = 175$ km/s as derived from the HeII 4686Å line (Fabrika & Bychkova 1990) and a binary inclination $i = 78^\circ$ (Eikenberry et al. 2001),

$$l_X = \frac{K_X}{\sin i} a_X = \frac{K_X}{\sin i} \frac{a_{orb}}{1+q} < \frac{K_X}{\sin i} a_{orb} = \quad (5)$$

$$178 \text{ km/s} \times 0.07 \text{ mas} \left(\frac{M}{40M_\odot} \right)^{1/3} \quad (6)$$

where $q = \frac{M_X}{M_*}$ is the mass ratio. The specific angular momentum of the donor star is even smaller, since $q < 1$ based on radial velocities (Hillwig & Gies 2008; Kubota et al. 2010) or other estimates of the mass ratio (Cherepashchuk et al. 2018; Bowler 2018). The extended outflows therefore seem to require a mechanism for transfer of substantial specific angular momentum to the outflowing material, which requires tidal or magnetic torques. We note that the inferred expansion velocity of the outflow ≈ 240 km/s corresponds to only ~ 0.02 mas/day, so that we do not expect to detect movement within the different epochs within the uncertainties.

Because the inner radius of the outflow ~ 0.1 mas $\sim a_{orb}$, it appears that it is launched from circumbinary material, disfavoring an origin from the accretion disk. We also disfavor such an origin based on theoretical arguments: centrifugal outflows from magnetic torques in the accretion disk itself require geometrically thin disks ($H \ll R$) threaded by vertical magnetic fields which dominate the pressure, whereas in SS 433 the disk is geometrically thick ($H \sim R$) and the extreme mass inflow $\dot{M} = 10^{-4} M_\odot/\text{yr}$ creates a large inward ram pressure as well as radiation pressure from supercritical accretion ($\dot{M} \gg \dot{M}_{Eddington}$). A more exotic possibility would be extraction of angular momentum from a neutron star through a magnetic propeller effect, in which transfer of angular momentum from the spinning neutron star to the flow can happen if the magnetospheric radius R_m is larger than the co-rotation radius R_{co} , leading the flow to be centrifugally ejected (Illarionov & Sunyaev 1975). Although the currently favored model for SS 433 is based on accretion-powered outflows from a massive stellar mass black hole (Fabrika 2004; Cherepashchuk et al. 2018; Bowler 2018), neutron star models for SS 433 have been considered in the past (e.g. Begelman et al. 1980; Begelman & Rees 1984), including the idea that it could be a supercritical propeller (Mineshige et al. 1991). In the latter scenario, R_m is smaller than the spherization radius R_{sp} so that a thick disk could still form (R_{sp} is the radius

within which the disk becomes geometrically thick from radiation pressure, determined from $L(R > R_{sp}) = L_{Eddington}$; Shakura & Sunyaev 1973). Our equatorial outflow model would require a launch radius $\gtrsim 4 \times 10^{10}$ cm for its speed not to exceed c ,

$$\text{which is comparable to } R_{sp} \approx 10^{10} \text{ cm} \frac{\dot{M}}{10^{-4} M_\odot/\text{yr}} \text{ in SS 433.}$$

However, for such a large magnetospheric radius to be inside the light cylinder of a neutron star would require a spin period $P \gtrsim 10$ s, deeming a propeller mechanism very unlikely (in addition, it would require very large $\gg 10^{15}$ G surface magnetic fields).

We instead favor that the outflow is driven from a circumbinary disk. There is strong evidence for a such a disk from optical spectroscopy (Blundell et al. 2008; Bowler 2010), which appears to be in Keplerian rotation at $\sim 1.5a_{orb}$ with a speed of ~ 250 km/s (Bowler 2018). It is probably fed by excretion through the Lagrangian points behind the compact object, donor star, or both. We note that the specific angular momentum of such disk is a few times higher than available in either binary component, so that its formation must also involve transfer of specific angular momentum. Just the same, there is strong evidence that this circumbinary disk is not stable: we see no evidence for equatorial material in the 2016 GRAVITY observation, where the asymmetric double-peaked Brγ line is instead aligned in the jet direction. We suggest that the equatorial structure we detected in optical interferometry traces the inner part of a centrifugally ejected disk, which implies there must be an efficient transfer of specific angular momentum from the binary to the disk, making it super-Keplerian by a factor ~ 7 , probably through tidal torques (e.g. Chen & Zeng 2009). It is then tempting to associate the enigmatic equatorial outflows sometimes detected in radio images to similar episodes of centrifugal ejection of the circumbinary disk. Interestingly, Goranskij (2017) reports on episodes of disappearance and reappearance of the eclipses and jets in SS 433, which they associate with the formation and ejection of a common envelope, and which could in turn be related to the formation and/or ejection of the circumbinary disk.

The feeding of the circumbinary disk removes angular momentum from the binary, and Cherepashchuk et al. (2018) has recently used the stability of the orbital period reported in Goranskij (2011) to constrain the mass ratio $q \gtrsim 0.6$. The ejection of the circumbinary disk we suggest here could also have important implications to the binary evolution. However, because it is most probably a transient structure, more observations are needed to understand its cadence and behavior, and that of the outflows in SS 433 in general. The two optical interferometric observations with GRAVITY so far have revealed extremely variable spatial structure to the line emission.

Finally, we note that the spherical wind component, with FWHM 2,000-3,000 km/s, surrounds the entire binary with a FWHM size $\sim 5-6$ mas (the fit size of the wind is much smaller for Epoch 1; however, this epoch suffers from severe blending with jet emission lines, so that its parameters are much more degenerate and difficult to constrain). The entire SS 433 system appears to be engulfed in an optically thin line emission envelope.

5. CONCLUSIONS

We have presented a second set of optical interferometry observations of the unique microquasar SS 433 with VLTI/GRAVITY. Here, we focused on the analysis of the near-infrared continuum and the Brγ stationary line.

We summarize our results as follows:

Table 3. Stationary Bry Model Fit Results

Parameter	unit	Model	2017-07-07 Epoch 1	2017-07-09 Epoch 2	2017-07-10 Epoch 3
Equatorial Structure Parameters					
R_{out}	mas	disk outflow	1.31 ± 0.07 0.93 ± 0.04	1.00 ± 0.06 0.71 ± 0.04	1.15 ± 0.07 0.65 ± 0.03
$\frac{R_{out}}{R_{in}}$	-	disk outflow	9.5 ± 0.2 10.9 ± 0.3	12.7 ± 0.2 7.0 ± 0.1	12.6 ± 0.2 7.3 ± 0.1
α	-	disk outflow	2.32 ± 0.07 0.6 ± 0.1	2.38 ± 0.05 2.19 ± 0.05	2.77 ± 0.04 2.45 ± 0.04
$v_{\phi}(R_{out})$	km/s	disk outflow	277 ± 2 284 ± 2	258 ± 2 215 ± 2	243 ± 2 216 ± 1
v_r	km/s	disk outflow	- 240 ± 2	- 236 ± 2	- 232 ± 2
i	deg	disk outflow	72 ± 1 69 ± 1	72.0 ± 0.6 56.7 ± 0.4	64.8 ± 0.4 52.2 ± 0.2
PA	deg	disk outflow	97 ± 2 86 ± 2	104 ± 4 96 ± 5	106 ± 4 107 ± 5
σ	-	disk outflow	0.349 ± 0.002 0.395 ± 0.001	0.375 ± 0.001 0.346 ± 0.002	0.356 ± 0.002 0.368 ± 0.001
M_{enc}^a	M_{\odot}	disk outflow	621 ± 34	416 ± 27	420 ± 23
Spherical Wind Parameters					
$FWHM_{wind}$	km/s	disk outflow	2975 ± 100 2582 ± 112	2810 ± 65 2494 ± 56	1952 ± 40 1809 ± 38
θ_{wind}	mas	disk outflow	0.7 ± 0.1 0.7 ± 0.1	5.3 ± 0.2 5.9 ± 0.2	5.9 ± 0.2 6.3 ± 0.3
Common Parameters					
v_{sys}	km/s	disk outflow	97 ± 1 66.1 ± 0.5	29.7 ± 0.5 47.1 ± 0.5	31.9 ± 0.3 31.2 ± 0.3
$\frac{\chi^2}{dof}$	-	disk outflow	2.7 2.7	1.5 1.6	1.0 1.0

Notes. ^(a) The enclosed mass is computed from R_{out} and $v_{\phi}(R_{out})$ for the case of a Keplerian disk.

1. The K band continuum is composed of an unresolved point source (accretion disk+donor star) and an extended FWHM ~ 7 mas structure. The latter is consistent with being an equatorial disk, but could also have a contribution from an extended spherical wind, both of which are seen in the Bry stationary line;
2. The model-independent emission centroids across the Bry line clearly point to it being dominated by an equatorial (perpendicular to the jets) structure in the 2017 observations, whereas in the previous GRAVITY observation in 2016 the emission was rather more aligned with the jets, suggestive of a bipolar outflow. The rotation direction of the outflow is retrograde relative to the jet precession, in accordance with the slaved disk precession model;
3. The equatorial structure is very extended and carries a specific angular momentum $\gtrsim 10\times$ greater than the one in either binary component. If interpreted as a disk in Keplerian rotation, it would imply an implausibly high enclosed mass $\sim 400M_{\odot}$. We suggest instead that it traces an outflow corresponding to the centrifugal ejection of a circumbinary disk, the existence of which has been inferred from optical spectroscopy. The non-detection of an equatorial structure in the

2016 observation suggests that such a disk can disappear. We suggest that the equatorial outflows typically seen in high-resolution radio images correspond to similar episodes of circumbinary disk ejection. The mechanism driving the specific angular momentum transfer necessary to make the disk super-Keplerian and centrifugally eject it is unclear, but possibly associated with tidal torques from the binary components;

4. The formation and ejection of the circumbinary disk could have an important effect on the binary evolution of SS 433 depending on their cadence. Future optical and radio interferometric observations capable of spatially resolving the outflows are needed to further study them;
5. In addition to the equatorial structure, the data also suggest a line component from a symmetric and extended spherical wind ~ 6 mas responsible for the high-velocity wings $\gtrsim 1000$ km/s of the line. The binary appears therefore to be engulfed in an optically thin and extended emission line envelope.

Acknowledgements. We thank the GRAVITY Co-Is, the GRAVITY Consortium and ESO for developing and operating the GRAVITY instrument. In particular, I.W. and J.D. thank the MPE GRAVITY team, in particular F. Eisenhauer, R. Genzel, S. Gillessen, T. Ott, O. Pfuhl and E. Sturm. We also thank the GRAVITY team members (W. Brandner, F. Eisenhauer, S. Hippler, M. Horrobin, T. Ott, T. Paumard, O. Pfuhl, O. Straub, E. Wieprecht) and ESO staff who were on the mountain during the observations. We also thank P. Kervella for comments on the paper. POP acknowledges financial support from the CNRS High Energy National Program (PNHE). POP and GD acknowledge financial support from the CNES. This research has made use of the Jean-Marie Mariotti Center SearchCal service ² co-developed by LAGRANGE and IPAG, CDS Astronomical Databases SIMBAD and VIZIER ³, NASA's Astrophysics Data System Bibliographic Services, NumPy (Van Der Walt et al. 2011) and matplotlib, a Python library for publication quality graphics (Hunter 2007).

References

Allen, D. A. 1979, *Nature*, 281, 284
 Begelman, M. C. & Rees, M. J. 1984, *MNRAS*, 206, 209
 Begelman, M. C., Sarazin, C. L., Hatchett, S. P., McKee, C. F., & Arons, J. 1980, *ApJ*, 238, 722
 Blundell, K. M. & Bowler, M. G. 2004, *ApJ*, 616, L159
 Blundell, K. M., Bowler, M. G., & Schmitzbreick, L. 2008, *ApJ*, 678, L47
 Blundell, K. M., Mioduszewski, A. J., Muxlow, T. W. B., Podsiadlowski, P., & Rupen, M. P. 2001, *ApJ*, 562, L79
 Bowler, M. G. 2010, *A&A*, 521, A81
 Bowler, M. G. 2018, *A&A*, 619, L4
 Brinkmann, W., Kawai, N., & Matsuoka, M. 1989, *A&A*, 218, L13
 Chelli, A., Duvert, G., Bourgès, L., et al. 2016, *A&A*, 589, A112
 Chen, W. & Zeng, Q. 2009, *Chinese Science Bulletin*, 54, 711
 Cherepashchuk, A. M., Postnov, K. A., & Belinski, A. A. 2018, *MNRAS*, 479, 4844
 Clark, D. H. & Murdin, P. 1978, *Nature*, 276, 44
 Doolin, S. & Blundell, K. M. 2009, *ApJ*, 698, L23
 Eikenberry, S. S., Cameron, P. B., Fierce, B. W., et al. 2001, *ApJ*, 561, 1027
 Fabian, A. C. & Rees, M. J. 1979, *MNRAS*, 187, 13P
 Fabrika, S. 2004, *Astrophysics and Space Physics Reviews*, 12, 1
 Fabrika, S. N. 1993, *MNRAS*, 261, 241
 Fabrika, S. N. & Bychkova, L. V. 1990, *A&A*, 240, L5
 Filippenko, A. V., Romani, R. W., Sargent, W. L. W., & Blandford, R. D. 1988, *AJ*, 96, 242
 Fuchs, Y., Koch Miramond, L., & Ábrahám, P. 2006, *A&A*, 445, 1041
 Goranskii, V. P., Esipov, V. F., & Cherepashchuk, A. M. 1998, *Astronomy Reports*, 42, 209
 Goranskij, V. 2011, *Peremennye Zvezdy*, 31 [arXiv:1110.5304]
 Goranskij, V. P. 2017, in *Astronomical Society of the Pacific Conference Series*, Vol. 510, *Stars: From Collapse to Collapse*, ed. Y. Y. Balega, D. O. Kudryavtsev, I. I. Romanyuk, & I. A. Yakunin, 466
 Gravity Collaboration, Abuter, R., Accardo, M., et al. 2017a, *A&A*, 602, A94
 Gravity Collaboration, Petrucci, P.-O., Waisberg, I., et al. 2017b, *A&A*, 602, L11

Hillwig, T. C. & Gies, D. R. 2008, *ApJ*, 676, L37
 Hunter, J. D. 2007, *Computing In Science & Engineering*, 9, 90
 Illarionov, A. F. & Sunyaev, R. A. 1975, *A&A*, 39, 185
 Kubota, K., Ueda, Y., Fabrika, S., et al. 2010, *ApJ*, 709, 1374
 Lapeyrière, V., Kervella, P., Lacour, S., et al. 2014, in *Proc. SPIE*, Vol. 9146, *Optical and Infrared Interferometry IV*, 91462D
 Leibowitz, E. M. 1984, *MNRAS*, 210, 279
 Luri, X., Brown, A. G. A., Sarro, L. M., et al. 2018, *A&A*, 616, A9
 Margon, B. 1984, *ARA&A*, 22, 507
 Margon, B., Ford, H. C., Grandi, S. A., & Stone, R. P. S. 1979, *ApJ*, 233, L63
 Marshall, H. L., Canizares, C. R., Hillwig, T., et al. 2013, *ApJ*, 775, 75
 Mineshige, S., Rees, M. J., & Fabian, A. C. 1991, *MNRAS*, 251, 555
 Mioduszewski, A. J., Rupen, M. P., Walker, R. C., Schillemat, K. M., & Taylor, G. B. 2004, in *Bulletin of the American Astronomical Society*, Vol. 36, *AAS/High Energy Astrophysics Division #8*, 967
 Monnier, J. D. & Allen, R. J. 2013, *Radio and Optical Interferometry: Basic Observing Techniques and Data Analysis*, ed. T. D. Oswalt & H. E. Bond, 325
 Paragi, Z., Fejes, I., Vermeulen, R. C., et al. 2002, in *Proceedings of the 6th EVN Symposium*, ed. E. Ros, R. W. Porcas, A. P. Lobanov, & J. A. Zensus, 263
 Paragi, Z., Vermeulen, R. C., Fejes, I., et al. 1999, *A&A*, 348, 910
 Perez M., S. & Blundell, K. M. 2009, *MNRAS*, 397, 849
 Roberts, W. J. 1974, *ApJ*, 187, 575
 Robinson, E. L., Froning, C. S., Jaffe, D. T., et al. 2017, *ApJ*, 841, 79
 Shakura, N. I. & Sunyaev, R. A. 1973, *A&A*, 24, 337
 Shklovskii, I. S. 1981, *Soviet Ast.*, 25, 315
 Stephenson, C. B. & Sanduleak, N. 1977, *ApJS*, 33, 459
 Stirling, A. M., Jowett, F. H., Spencer, R. E., et al. 2002, *MNRAS*, 337, 657
 van den Heuvel, E. P. J., Ostriker, J. P., & Petterson, J. A. 1980, *A&A*, 81, L7
 Van Der Walt, S., Colbert, S. C., & Varoquaux, G. 2011, *Computing in Science & Engineering*, 13, 22
 Vermeulen, R. C., Schilizzi, R. T., Spencer, R. E., Romney, J. D., & Fejes, I. 1993, *A&A*, 270, 177
 Waisberg, I., Dexter, J., Pfuhl, O., et al. 2017, *ApJ*, 844, 72
 Whitmore, D. P. & Matese, J. J. 1980, *MNRAS*, 193, 707
 Zwitter, T., Calvani, M., & D'Odorico, S. 1991, *A&A*, 251, 92

² Available at <http://www.jmmc.fr/searchcal>

³ Available at <http://cdsweb.u-strasbg.fr/>

Appendix A: Full Data and Model Fits

Here we show the data (spectrum, differential visibility phases and amplitudes) and best fits for the "outflow" model for the three epochs of the 2017 observations and for all baselines. The solid lines show the models without the blended jet emission lines, whereas the dashed lines show the full combined model (as the fits are done). For the jet models and results, we refer to the companion paper on the jets, Waisberg et al., sub. The projected length and position angle of each baseline is indicated.

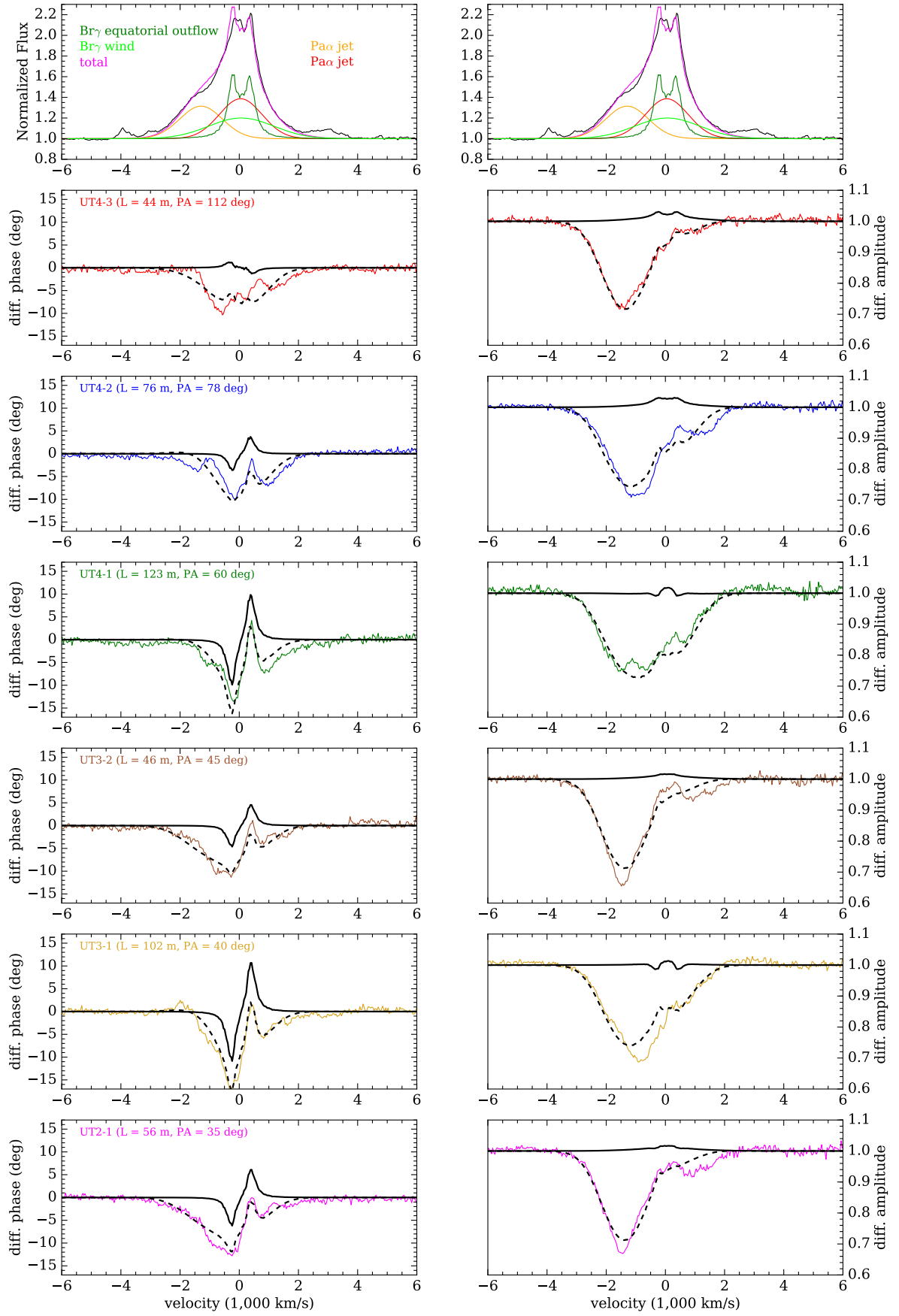


Fig. A.1 Data and best-fit "outflow" model for Epoch 1.

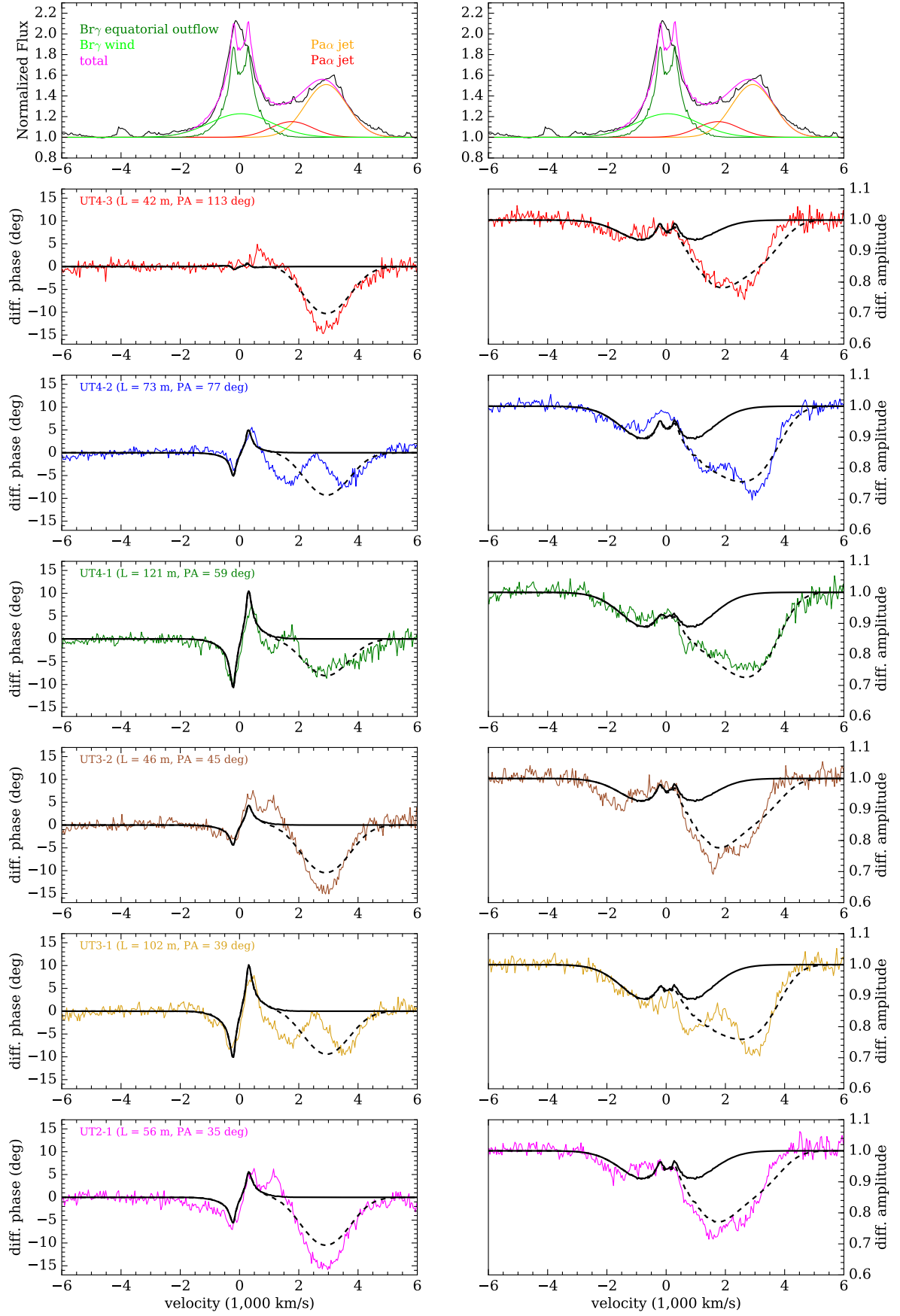


Fig. A.2. Data and best fit "outflow" model for Epoch 2.

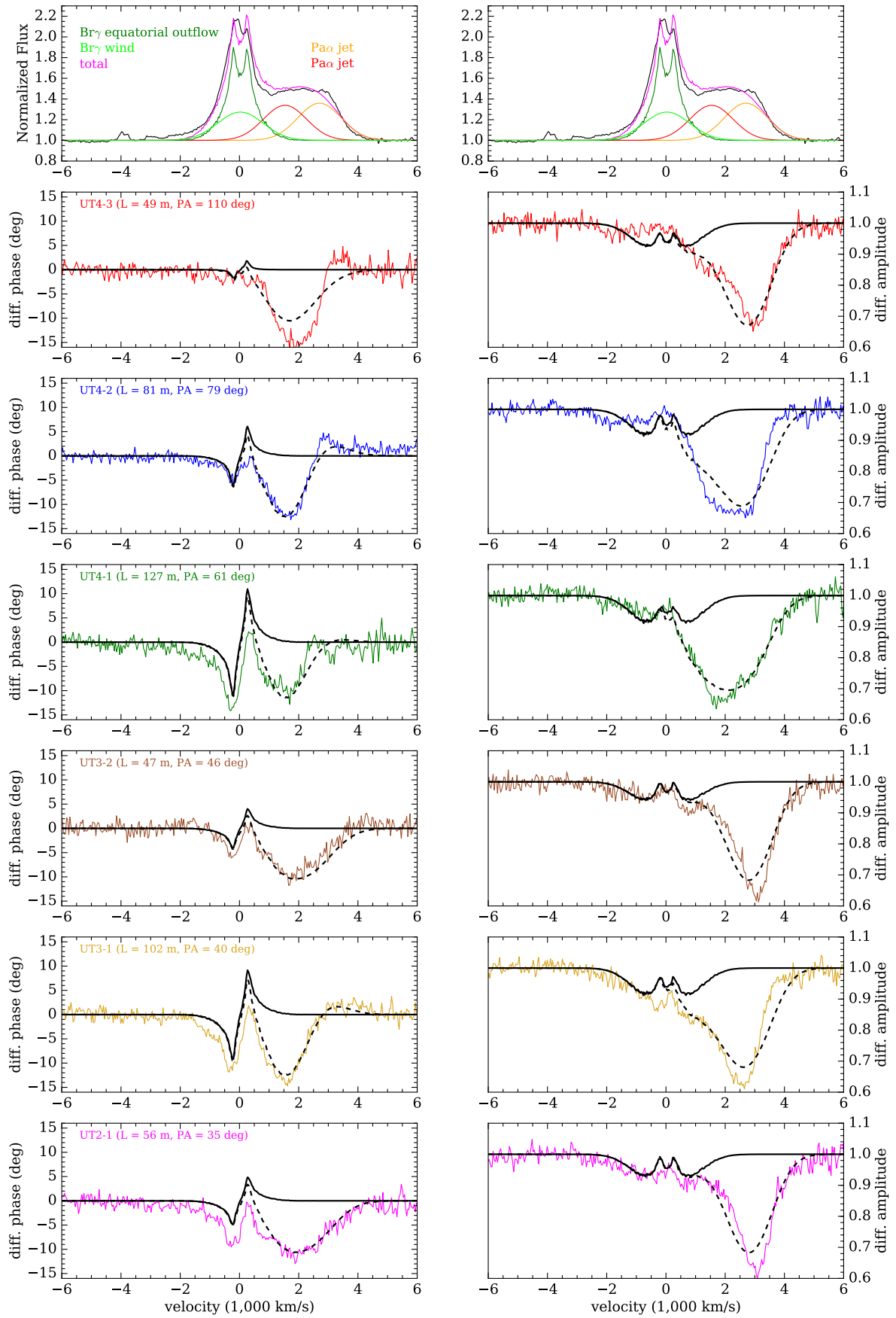


Fig. A.3. Data and best-fit "outflow" model for Epoch 3.